

# Shape transition and fluctuation in neutron-rich Cr isotopes around $N = 40$

Koichi Sato,<sup>1</sup> Nobuo Hinohara,<sup>2,1</sup> Kenichi Yoshida,<sup>3,4</sup>  
Takashi Nakatsukasa,<sup>1</sup> Masayuki Matsuo,<sup>3,4</sup> and Kenichi Matsuyanagi<sup>1,5</sup>

<sup>1</sup>*RIKEN Nishina Center, Wako 351-0198, Japan*

<sup>2</sup>*Department of Physics and Astronomy, University of North Carolina, Chapel Hill, North Carolina 27599-3255, USA*

<sup>3</sup>*Graduate School of Science and Technology, Niigata University, Niigata 950-2181, Japan*

<sup>4</sup>*Department of Physics, Faculty of Science, Niigata University, Niigata 950-2181, Japan*

<sup>5</sup>*Yukawa Institute for Theoretical Physics, Kyoto University, Kyoto 606-8502, Japan*

(Dated: June 12, 2021)

The spherical-to-prolate shape transition in neutron-rich Cr isotopes from  $N = 34$  to 42 is studied by solving the collective Schrödinger equation for the five-dimensional quadrupole collective Hamiltonian. The collective potential and inertial functions are microscopically derived with use of the constrained Hartree-Fock-Bogoliubov plus local quasiparticle random-phase approximation method. Nature of the quadrupole collectivity of low-lying states is discussed by evaluating excitation spectra and electric quadrupole moments and transition strengths. The result of calculation indicates that Cr isotopes around  $^{64}\text{Cr}$  are prolately deformed but still possess transitional character; large-amplitude shape fluctuations dominate in their low-lying states.

PACS numbers: 21.10.Ky, 21.10.Re, 21.60.Ev, 21.60.Jz, 27.50.+e

## I. INTRODUCTION

Recent experiments on neutron-rich Cr isotopes show that quadrupole collectivity appreciably develops toward  $^{64}\text{Cr}$  with  $N = 40$  [1–6]. Going from  $^{58}\text{Cr}$  to  $^{64}\text{Cr}$ , the excitation energy of the first excited  $2_1^+$  state decreases and  $R_{4/2}$ , the ratio of the excitation energy of the  $4_1^+$  state to that of the  $2_1^+$  state, increases. These data seem to indicate that a quantum phase transition from the spherical to deformed shapes takes place near  $N = 40$ . The microscopic origin of the enhanced quadrupole collectivity toward  $N = 40$  has been actively discussed from various theoretical approaches: the Hartree-Fock-Bogoliubov (HFB) mean-field calculations using the Skyrme force [8] or the Gogny force [9], the spherical shell-model [7, 10], and the projected deformed shell model [11]. These calculations have clarified the important role of the neutron  $g_{9/2}$  and  $d_{5/2}$  single-particle levels in the emergence of the quadrupole collectivity near  $N = 40$ . Although the spherical shell model calculations reproduce the experimental data rather well, the character of the quadrupole deformation, especially, the distinction between the equilibrium shape and shape fluctuations around it is not sufficiently clear.

In this paper, we investigate the nature of the quadrupole collectivity in low-lying states of the neutron-rich Cr isotopes  $^{58-64}\text{Cr}$  using an approach that treats the quadrupole deformations as dynamical variables. Thus, the distinction of the equilibrium shape and shape fluctuations is transparent. The deformation energy curve with respect to the axial quadrupole deformation was obtained in the Skyrme HFB mean-field calculation [8], which shows that the quadrupole instability occurs around  $N = 38 - 42$ . However, the deformed minima are extremely shallow in these nuclei, suggesting a transitional character. In such transitional situations, one naturally expects that large-amplitude shape

fluctuations play an important role in determining the properties of low-lying excited states. Therefore, we take the five-dimensional (5D) quadrupole collective Hamiltonian approach [12], which is capable of describing the large-amplitude quadrupole shape fluctuations associated with the quantum shape transition. It enables us to treat a variety of quadrupole deformation phenomena (vibrational, spherical-prolate transitional, rotational,  $\gamma$ -unstable, triaxial, oblate-prolate shape-coexistent situations, etc.) on an equal footing. Dynamical variables of the 5D quadrupole collective Hamiltonian approach are the magnitude and triaxiality of quadrupole deformation ( $\beta, \gamma$ ) and the three Euler angles. To explicitly indicate the two vibrational and three rotational degrees of freedom, we call it (2+3)D, hereafter. The 5D collective Hamiltonian is characterized by seven functions: the collective potential, three vibrational inertial functions (also called vibrational masses), and three rotational inertial functions. To evaluate the inertial functions, the Inglis-Belyaev (IB) cranking formula has been conventionally used. However, it is well known that the contribution of the time-odd components of the moving mean field is ignored in the IB cranking formula, which leads to the overestimation of excitation energies [14, 15].

The constrained Hartree-Fock-Bogoliubov plus local quasiparticle random-phase approximation (CHFB+LQRPA) method [16] is a method which can overcome the shortcoming of the IB cranking formula. It is derived on the basis of the adiabatic self-consistent collective coordinate (ASCC) method [15, 17, 18] by assuming that there is a one-to-one mapping from a point on the collective submanifold embedded in the large-dimensional time-dependent HFB phase space to a point in the  $(\beta, \gamma)$  deformation space. In the CHFB+LQRPA method, the inertial functions are derived by transforming the local canonical coordinates determined by the LQRPA normal modes

to the  $(\beta, \gamma)$  degrees of freedom. This method has been successfully applied to several phenomena: shape coexistence/fluctuation in Se and Kr isotopes [14, 16, 19], development of triaxial deformation in  $^{110}\text{Mo}$  [20], and shape fluctuations in neutron-rich Mg isotopes [21]. Use of the Skyrme energy density functional in solving the CHFB+LQRPA equations has also been initiated for the axially symmetric quadrupole Hamiltonian [22]. In this paper, we solve the LQRPA equations with use of the pairing-plus-quadrupole (P+Q) model [12] including the quadrupole pairing interaction. For the collective Hamiltonian quantized according to the Pauli prescription, we solve the collective Schrödinger equation to obtain the excitation energies, vibrational wave functions,  $E2$ -transition strengths and moments.

This paper is organized as follows. We recapitulate the theoretical framework in Sec. II. In Sec. III, we present results of calculation for  $^{58-66}\text{Cr}$  and discuss the nature of quadrupole collectivity in their low-lying states. To examine the role of the shape fluctuations toward the triaxial shape ( $\gamma$  degree of freedom), we also carry out calculations imposing the axial symmetry on the nuclear shape. We call it (1+2)D calculation indicating that the one vibrational degree of freedom in the  $\beta$  direction and the two Euler angles describing rotations perpendicular to the symmetry axis are taken into account. Comparing results of such a restricted calculation with those of the (2+3)D calculation, we shall see the importance of the triaxial shape fluctuations. We carry out a similar calculation also for  $^{66}\text{Fe}$  to compare with  $^{64}\text{Cr}$ . We then discuss similarities and differences of the quadrupole shape transition near  $^{64}\text{Cr}$  with  $N = 40$  and that near  $^{32}\text{Mg}$  with  $N = 20$ . Conclusions are given in Sec. IV.

## II. THEORETICAL FRAMEWORK

In this section, we briefly summarize the framework of our collective Hamiltonian approach. See Ref. [16] for details.

### A. 5D quadrupole collective Hamiltonian

The 5D quadrupole collective Hamiltonian is given by

$$\mathcal{H}_{\text{coll}} = T_{\text{vib}} + T_{\text{rot}} + V(\beta, \gamma), \quad (1)$$

$$T_{\text{vib}} = \frac{1}{2}D_{\beta\beta}(\beta, \gamma)\dot{\beta}^2 + D_{\beta\gamma}(\beta, \gamma)\dot{\beta}\dot{\gamma} + \frac{1}{2}D_{\gamma\gamma}(\beta, \gamma)\dot{\gamma}^2, \quad (2)$$

$$T_{\text{rot}} = \frac{1}{2} \sum_{k=1}^3 \mathcal{J}_k(\beta, \gamma) \omega_k^2, \quad (3)$$

where  $T_{\text{vib}}$  and  $T_{\text{rot}}$  represent the vibrational and rotational kinetic energies, while  $V$  the collective potential energy. The moments of inertia are parametrized as  $\mathcal{J}_k(\beta, \gamma) = 4\beta^2 D_k(\beta, \gamma) \sin^2 \gamma_k$  with  $\gamma_k = \gamma - 2\pi k/3$ .

The collective potential and inertial functions are determined with the CHFB+LQRPA method as explained in the next subsection. Once they are determined as functions of  $(\beta, \gamma)$ , we quantize the collective Hamiltonian according to the Pauli prescription. The collective Schrödinger equation for the quantized collective Hamiltonian is given by

$$\{\hat{T}_{\text{vib}} + \hat{T}_{\text{rot}} + V\} \Psi_{\alpha IM}(\beta, \gamma, \Omega) = E_{\alpha I} \Psi_{\alpha IM}(\beta, \gamma, \Omega), \quad (4)$$

where

$$\begin{aligned} \hat{T}_{\text{vib}} = & \frac{-1}{2\sqrt{WR}} \left\{ \frac{1}{\beta^4} \left[ \left( \partial_{\beta} \beta^2 \sqrt{\frac{R}{W}} D_{\gamma\gamma} \partial_{\beta} \right) \right. \right. \\ & \left. \left. - \partial_{\beta} \left( \beta^2 \sqrt{\frac{R}{W}} D_{\beta\gamma} \partial_{\gamma} \right) \right] \right. \\ & + \frac{1}{\beta^2 \sin 3\gamma} \left[ -\partial_{\gamma} \left( \sqrt{\frac{R}{W}} \sin 3\gamma D_{\beta\gamma} \partial_{\beta} \right) \right. \\ & \left. \left. + \partial_{\gamma} \left( \sqrt{\frac{R}{W}} \sin 3\gamma D_{\beta\beta} \partial_{\gamma} \right) \right] \right\} \end{aligned} \quad (5)$$

and

$$\hat{T}_{\text{rot}} = \sum_k \frac{\hat{J}_k^2}{2\mathcal{J}_k}. \quad (6)$$

Here,  $R(\beta, \gamma)$  and  $W(\beta, \gamma)$  are defined as

$$R(\beta, \gamma) = D_1(\beta, \gamma) D_2(\beta, \gamma) D_3(\beta, \gamma), \quad (7)$$

$$W(\beta, \gamma) = \{ D_{\beta\beta}(\beta, \gamma) D_{\gamma\gamma}(\beta, \gamma) - [D_{\beta\gamma}(\beta, \gamma)]^2 \} \beta^{-2}. \quad (8)$$

The collective wave function  $\Psi_{\alpha IM}(\beta, \gamma, \Omega)$  is specified by the total angular momentum  $I$ , its projection onto the  $z$ -axis of the laboratory frame  $M$ , and  $\alpha$  distinguishing the states with the same  $I$  and  $M$ . It can be written as a sum of products of the vibrational and rotational wave functions:

$$\Psi_{\alpha IM}(\beta, \gamma, \Omega) = \sum_{K=\text{even}} \Phi_{\alpha IK}(\beta, \gamma) \langle \Omega | IMK \rangle, \quad (9)$$

where

$$\langle \Omega | IMK \rangle = \sqrt{\frac{2I+1}{16\pi^2(1+\delta_{K0})}} [\mathcal{D}_{MK}^I(\Omega) + (-)^I \mathcal{D}_{M-K}^I(\Omega)]. \quad (10)$$

$\mathcal{D}_{MK}^I$  is the Wigner rotation matrix and  $K$  is the projection of the angular momentum onto the  $z$ -axis in the body-fixed frame. The summation over  $K$  is taken from 0 to  $I$  for even  $I$  and from 2 to  $I-1$  for odd  $I$ .

The vibrational wave functions in the body-fixed frame,  $\Phi_{\alpha IK}(\beta, \gamma)$ , are normalized as

$$\int d\beta d\gamma |\Phi_{\alpha I}(\beta, \gamma)|^2 |G(\beta, \gamma)|^{\frac{1}{2}} = 1, \quad (11)$$

where

$$|\Phi_{\alpha I}(\beta, \gamma)|^2 \equiv \sum_{K=\text{even}} |\Phi_{\alpha IK}(\beta, \gamma)|^2, \quad (12)$$

and the volume element  $|G(\beta, \gamma)|$  is given by

$$|G(\beta, \gamma)| = 4\beta^8 W(\beta, \gamma) R(\beta, \gamma) \sin^2 3\gamma. \quad (13)$$

The symmetries and boundary conditions of the collective Hamiltonian and wave functions are discussed in Ref. [23].

## B. The CHFb+LQRPA method

We determine the collective potential and inertial functions with the CHFb+LQRPA method. We first solve the CHFb equation

$$\delta \langle \phi(\beta, \gamma) | \hat{H}_{\text{CHFb}}(\beta, \gamma) | \phi(\beta, \gamma) \rangle = 0, \quad (14)$$

$$\hat{H}_{\text{CHFb}} = \hat{H} - \sum_{\tau} \lambda^{(\tau)} \hat{N}^{(\tau)} - \sum_m \mu^{(m)} \hat{D}_{2m}^{(+)} \quad (15)$$

with the constraints on the particle numbers and quadrupole deformation parameters:

$$\langle \phi(\beta, \gamma) | \hat{N}^{(\tau)} | \phi(\beta, \gamma) \rangle = N_0^{(\tau)}, \quad (\tau = n, p) \quad (16)$$

$$\langle \phi(\beta, \gamma) | \hat{D}_{2m}^{(+)} | \phi(\beta, \gamma) \rangle = D_{2m}^{(+)}, \quad (m = 0, 2). \quad (17)$$

Here,  $\hat{D}_{2m}^{(+)}$  denotes Hermitian quadrupole operators,  $\hat{D}_{20}$  and  $(\hat{D}_{22} + \hat{D}_{2-2})/2$  for  $m = 0$  and  $2$ , respectively. Then, we solve the LQRPA equations for vibration on top of the CHFb states obtained above,

$$\delta \langle \phi(\beta, \gamma) | [\hat{H}_{\text{CHFb}}(\beta, \gamma), \hat{Q}^i(\beta, \gamma)] - \frac{1}{i} \hat{P}_i(\beta, \gamma) | \phi(\beta, \gamma) \rangle = 0, \quad (18)$$

$$\delta \langle \phi(\beta, \gamma) | [\hat{H}_{\text{CHFb}}(\beta, \gamma), \frac{1}{i} \hat{P}_i(\beta, \gamma)] - C_i(\beta, \gamma) \hat{Q}^i(\beta, \gamma) | \phi(\beta, \gamma) \rangle = 0, \quad (i = 1, 2). \quad (19)$$

The infinitesimal generators,  $\hat{Q}^i(\beta, \gamma)$  and  $\hat{P}_i(\beta, \gamma)$ , are locally defined at every point of the  $(\beta, \gamma)$  deformation space. The quantity  $C_i(\beta, \gamma)$  is related to the eigenfrequency  $\omega_i(\beta, \gamma)$  of the local normal mode through  $\omega_i^2(\beta, \gamma) = C_i(\beta, \gamma)$ . It is worth noting that these equations are valid also for regions with negative curvature ( $C_i(\beta, \gamma) < 0$ ) where  $\omega_i(\beta, \gamma)$  takes an imaginary value.

We assume that a 2D collective submanifold is embedded in a large-dimensional TDHFB configuration space and define local canonical coordinates  $(q_1, q_2)$  on it. We also assume that there is a one-to-one mapping between  $(q_1, q_2)$  and  $(\beta, \gamma)$ . By performing a similarity transformation of  $(q_1, q_2)$ , the vibrational kinetic energy can be written, without loss of generality, as

$$T_{\text{vib}} = \frac{1}{2} \sum_{i=1,2} \dot{q}_i^2, \quad (20)$$

which can be transformed to

$$T_{\text{vib}} = \frac{1}{2} M_{00} [\dot{D}_{20}^{(+)}]^2 + M_{02} \dot{D}_{20}^{(+)} \dot{D}_{22}^{(+)} + \frac{1}{2} M_{22} [\dot{D}_{22}^{(+)}]^2, \quad (21)$$

in terms of the time derivatives of  $D_{2m}^{(+)}$ . The vibrational masses with respect to  $D_{2m}^{(+)}$  are given by

$$M_{mm'}(\beta, \gamma) = \sum_{i=1,2} \frac{\partial q^i}{\partial D_{2m}^{(+)}} \frac{\partial q^i}{\partial D_{2m'}^{(+)}}. \quad (22)$$

The partial derivatives can be easily evaluated as

$$\begin{aligned} \frac{\partial D_{20}^{(+)}}{\partial q^i} &= \frac{\partial}{\partial q^i} \langle \phi(\beta, \gamma) | \hat{D}_{20}^{(+)} | \phi(\beta, \gamma) \rangle \\ &= \langle \phi(\beta, \gamma) | [\hat{D}_{20}^{(+)}, \frac{1}{i} \hat{P}_i(\beta, \gamma)] | \phi(\beta, \gamma) \rangle, \end{aligned} \quad (23)$$

$$\begin{aligned} \frac{\partial D_{22}^{(+)}}{\partial q^i} &= \frac{\partial}{\partial q^i} \langle \phi(\beta, \gamma) | \hat{D}_{22}^{(+)} | \phi(\beta, \gamma) \rangle \\ &= \langle \phi(\beta, \gamma) | [\hat{D}_{22}^{(+)}, \frac{1}{i} \hat{P}_i(\beta, \gamma)] | \phi(\beta, \gamma) \rangle, \end{aligned} \quad (24)$$

without need of numerical derivatives. Through the definition of  $(\beta, \gamma)$  in terms of  $(D_{20}^{(+)}, D_{22}^{(+)})$ , the vibrational inertial functions  $(D_{\beta\beta}, D_{\gamma\gamma}, D_{\beta\gamma})$  with respect to  $(\beta, \gamma)$  are easily obtained from  $(M_{00}, M_{02}, M_{22})$  [16]. To select two collective normal modes among the LQRPA modes obtained by solving Eqs. (18) and (19), we employ the minimal metric criterion [16].

The rotational moments of inertia are calculated by solving the LQRPA equations for rotation on each CHFb state:

$$\delta \langle \phi(\beta, \gamma) | [\hat{H}_{\text{CHFb}}, \hat{\Psi}_k(\beta, \gamma)] - \frac{1}{i} (\mathcal{J}_k)^{-1} \hat{I}_k | \phi(\beta, \gamma) \rangle = 0, \quad (25)$$

$$\langle \phi(\beta, \gamma) | [\hat{\Psi}_k(\beta, \gamma), \hat{I}_{k'}] | \phi(\beta, \gamma) \rangle = i \delta_{kk'}, \quad (26)$$

where  $\hat{I}_k$  and  $\hat{\Psi}_k(\beta, \gamma)$  represent the angular momentum and the rotational angle operators with respect to the principal axes associated with the CHFb state  $|\phi(\beta, \gamma)\rangle$ . This is an extension of the Thouless-Valatin equation [24] for the HFB equilibrium state to non-equilibrium CHFb states. We call  $\mathcal{J}_k(\beta, \gamma)$  determined by the above equations ‘LQRPA moments of inertia.’

We solve the collective Schrödinger equation (4) to obtain excitation energies and vibrational wave functions. Then, electric transition strengths and moments are readily calculated (see Ref. [19] for details).

## C. Details of the numerical calculation

In this study, we adopt a version of the pairing-plus-quadrupole (P+Q) model [12] including the quadrupole

pairing interaction as well as the monopole pairing interaction. We take two harmonic-oscillator shells with  $N_{sh}=3, 4$  and  $N_{sh}=2, 3$  for neutrons and protons, respectively. The single-particle energies are determined from those obtained with the constrained Skyrme-HFB calculations at the spherical shape using the HFBTHO code [25]. In these Skyrme-HFB calculations, we employ the SkM\* functional and the volume-type pairing with the pairing strength  $V_0 = -180 \text{ MeV fm}^{-3}$ . The pairing strength has been adjusted such that the calculated neutron pairing gaps at the HFB minima reproduce the experimental gaps in  $^{58-64}\text{Cr}$ . The single-particle energies are scaled with the effective mass of the SkM\* functional  $m^*/m = 0.79$ , because the P+Q model is designed to be used for single particles whose mass is the bare nucleon mass.

The parameters of the P+Q model are determined as follows. For  $^{62}\text{Cr}$ , the monopole pairing strengths  $G_0^\tau$  ( $\tau = n, p$ ) and quadrupole interaction strength  $\chi$  are determined to approximately reproduce the HFB equilibrium deformation and the pairing gaps at the spherical and HFB equilibrium shapes. For the other nuclei  $^{58,60,64,66}\text{Cr}$  and  $^{66}\text{Fe}$ , we assume the simple mass number dependence according to Baranger and Kumar [12]:  $G_0^\tau \sim A^{-1}$  and  $\chi' \equiv \chi b^4 \sim A^{-5/3}$  ( $b$  denotes the oscillator-length parameter). We follow the Sakamoto-Kishimoto prescription to determine the strengths of the quadrupole pairing [26]. We omit the Fock term as in the conventional treatment of the P+Q model.

The CHF+LQRPA equations are solved at  $60 \times 60$  mesh points in the  $(\beta, \gamma)$  plane defined by

$$\beta_i = (i - 0.5) \times 0.01, \quad (i = 1, \dots, 60), \quad (27)$$

$$\gamma_j = (j - 0.5) \times 1^\circ, \quad (j = 1, \dots, 60). \quad (28)$$

For the calculation of the  $E2$  transitions and moments, we use the effective charges  $(e_{\text{eff}}^{(n)}, e_{\text{eff}}^{(p)}) = (0.5, 1.5)$ .

### III. RESULTS AND DISCUSSION

In this section, we present the numerical results for  $^{58-66}\text{Cr}$  and discuss the nature of quadrupole collectivity in their low-lying states. The results for  $^{64}\text{Cr}$  are compared with those for the neighboring nucleus  $^{66}\text{Fe}$  with  $N = 40$ . We furthermore discuss the similarities and differences with Mg isotopes around  $N = 20$ .

#### A. Collective potentials and inertial functions

We plot the collective potential  $V(\beta, \gamma)$  calculated for  $^{58-66}\text{Cr}$  in Fig. 1. The location of the absolute minimum is indicated by the (blue) circle. In  $^{58}\text{Cr}$ , the absolute minimum is located at a nearly spherical shape. Although the minimum shifts to larger deformation in  $^{60}\text{Cr}$ , the collective potential is extremely soft in the  $\beta$  direction. A more pronounced local minimum appears at

larger deformation in  $^{62}\text{Cr}$ , and the minimum becomes even deeper in  $^{64}\text{Cr}$ . In  $^{66}\text{Cr}$ , the collective potential becomes slightly softer than in  $^{64}\text{Cr}$ . These potential energy surfaces indicate that a quantum shape transition from a spherical to a prolately deformed shape takes place along the isotopic chain toward  $N = 40$ . In Fig. 2, we plot the Nilsson diagrams of neutrons and protons as functions of  $\beta$  calculated for  $^{62}\text{Cr}$  as in Ref. [13]. This is similar to Figs. 5(a) and 5(b) in Ref. [8].

In Fig. 3, we plot the neutron and proton monopole pairing gaps  $\Delta_0^{(n)}(\beta, \gamma)$  and  $\Delta_0^{(p)}(\beta, \gamma)$ , the vibrational inertial function  $D_{\beta\beta}(\beta, \gamma)$ , and the rotational moment of inertia  $\mathcal{J}_1(\beta, \gamma)$ , calculated for  $^{62}\text{Cr}$ . Figures 3 (c) clearly shows that the vibrational inertial function is well correlated with the magnitudes of the pairing gaps:  $D_{\beta\beta}(\beta, \gamma)$  becomes small in the near spherical region where  $\Delta_0^{(n)}$  and  $\Delta_0^{(p)}$  take large values. One might be concerned for complicated behaviors of  $D_{\beta\beta}(\beta, \gamma)$  in the strongly deformed region. However, they hardly affect low-lying states, because the collective potential energy is very high there and contributions from this region to the vibrational wave functions are negligibly small. Figures 3 (d) clearly indicates that the rotational moment of inertia also has a strong correlation with the pairing gaps. It takes the maximum value in the prolate region around  $\beta \simeq 0.35$ . Both the neutron and proton pairing gaps become small there due to the deformed shell gaps for  $N = 38$  and  $Z = 24$ , see Fig. 2. In particular, the proton pairing gap almost vanishes. It results in the increase of the moment of inertia. As we shall see later, this enhancement promotes the localization of the vibrational wave functions in the  $(\beta, \gamma)$  plane for excited states with non-zero angular momenta. The rotational and vibrational inertial functions for the other isotopes are qualitatively the same as those for  $^{62}\text{Cr}$ . The enhancement of the moments of inertia mentioned above grows gradually with increasing neutron number up to  $N = 40$ .

#### B. Yrast states in $^{58-66}\text{Cr}$

We show in Fig. 4 the excitation energies of the  $2_1^+$  and  $4_1^+$  states, their ratios  $R_{4/2}$ , the  $E2$  transition strengths  $B(E2; 2_1^+ \rightarrow 0_1^+)$ , and the spectroscopic quadrupole moments of the  $2_1^+$  states, together with the available experimental data. The decrease in the excitation energies of the  $2_1^+$  and  $4_1^+$  states toward  $N = 40$  and the increase in their ratio from  $N = 36$  to  $N = 40$  are well described and indicate that the nature of the quadrupole collectivity gradually changes from vibrational to rotational as the neutron number increases. However, the ratio  $R_{4/2}$  at  $N = 40$  is still 2.68, which is considerably smaller than the rigid-rotor value 3.33. The  $B(E2)$  values and spectroscopic quadrupole moments  $Q(2_1^+)$  also suggest the onset of deformation:  $B(E2)$  increases and the magnitude of the spectroscopic quadrupole moments, which has a negative sign indicating a prolate shape, increase

with increasing neutron number and both of them reach a maximum at  $N = 40$ . In Fig. 4, we also plot the results of the (1+2)D calculations, in which only the axially symmetric deformation is taken into account. Physical meaning of the differences between the (2+3)D and (1+2)D calculations will be discussed in a subsequent subsection.

In Table I, we compare the results for  $^{64}\text{Cr}$  with those for  $^{66}\text{Fe}$ . Experimental data indicate that the quadrupole collectivity is stronger in  $^{64}\text{Cr}$  than in  $^{66}\text{Fe}$ : the smaller  $E(2_1^+)$  and the larger  $R_{4/2}$  and  $B(E2)$  values for  $^{64}\text{Cr}$  than those for  $^{66}\text{Fe}$ . Our calculation reproduces these features quite well.

We depict in Figs. 5 and 6 the squared vibrational wave functions multiplied by  $\beta^4$  for the  $0_1^+$ ,  $2_1^+$  and  $4_1^+$  states in  $^{58-66}\text{Cr}$  and those without the  $\beta^4$  factor for the  $0_1^+$  and  $2_1^+$  states in  $^{60}\text{Cr}$  and  $^{64}\text{Cr}$ , respectively. The  $\beta^4$  factor comes from the volume element and carries its dominant  $\beta$  dependence (see Eqs. (11) and (13)). The wave functions look quite different between the two cases. For instance, while the non-weighted  $0_1^+$  wave function for  $^{60}\text{Cr}$  shown in Fig. 6 distributes around the spherical shape, the  $\beta^4$  factor changes it to the arcuate pattern seen in Fig. 5. In  $^{58}\text{Cr}$  and  $^{60}\text{Cr}$ , the  $\beta^4$ -weighted  $0_1^+$  wave functions exhibit arcuate distributions around  $\beta = 0.2$  covering the entire  $\gamma$  region. Closely looking, one finds that, while the distribution for  $^{58}\text{Cr}$  is almost uniform in the  $\gamma$  direction, it is slightly leaning to the prolate side for  $^{60}\text{Cr}$ .

With increasing neutron number, the  $0_1^+$  wave function localizes more and more on the prolate side, reflecting the deepening of the prolate minima (see the collective potential in Fig. 1). In  $^{62}\text{Cr}$ , the  $0_1^+$  wave function still spreads over the entire  $\gamma$  region, although it has a clear concentration on the prolate side. In  $^{64}\text{Cr}$ , one can see a distinct peak around the prolate potential minimum, and the  $0_1^+$  wave function is most localized at  $^{64}\text{Cr}$ . The vibrational wave functions clearly indicate the shape transition from spherical to prolate along the isotopic chain.

For all these isotopes, one can see that the prolate peak grows with increasing angular momentum. This is due to the enhancement of the moments of inertia on the prolate side we have already seen in Fig. 3. Even in  $^{58}\text{Cr}$  whose ground state is rather spherical, the  $2_1^+$  and  $4_1^+$  states are weakly localized on the prolate side, which results in the finite spectroscopic quadrupole moment shown in Fig. 4.

TABLE I: Excitation energies of the  $2_1^+$  state  $E(2_1^+)$  in keV, the ratios  $R_{4/2}$  of  $E(4_1^+)$  to  $E(2_1^+)$ , and  $B(E2; 2_1^+ \rightarrow 0_1^+)$  in Weisskopf units for  $^{64}\text{Cr}$  and  $^{66}\text{Fe}$ . Experimental data are taken from Ref. [6, 29].

	$E(2_1^+)$	Calc.		$E(2_1^+)$	Exp.	
		$R_{4/2}$	$B(E2)$		$R_{4/2}$	$B(E2)$
$^{64}\text{Cr}$	386	2.68	28.8	420	2.69	
$^{66}\text{Fe}$	685	2.29	15.5	573	2.47	21.0

In  $^{64}\text{Cr}$ , the  $2_1^+$  and  $4_1^+$  wave functions are well localized on the prolate side, although the ground state wave function still exhibit non-negligible shape fluctuation in the  $\gamma$  direction. Due to the growth of localization of the wave functions, higher angular momentum states acquire more rotor-like character than the ground state. This fact can be quantified by calculating the ratio

$$R_{6/4/2} \equiv (E(6_1^+) - E(2_1^+))/(E(4_1^+) - E(2_1^+)). \quad (29)$$

For instance,  $R_{6/4/2} = 2.42$  for  $^{64}\text{Cr}$ , which is fairly close to the rigid-rotor value 2.57, although the calculated  $R_{4/2}$  is 2.67 which is far from the rigid-rotor value 3.33. These results clearly indicate the importance of dynamical effects of rotation on the nuclear shape.

Lenzi et al. [7] evaluated the intrinsic quadrupole moments  $Q_{\text{int}}(I)$  for the yrast states of  $^{62-66}\text{Cr}$  using the spectroscopic quadrupole moments  $Q(I)$  obtained in their shell-model calculation and the well-known relation between them for the axially symmetric deformation with  $K=0$ . The resulting  $Q_{\text{int}}(I)$  stay approximately constant along the yrast sequences in  $^{62,64,66}\text{Cr}$ , and they interpreted this as a fingerprint of a rigid rotor behavior. We have evaluated  $Q_{\text{int}}(I)$  in the same way as Lenzi et al. but using our calculated  $Q(I)$ . The resulting  $Q_{\text{int}}(I)$  values are similar to those of Lenzi et al. We feel, however, that this fact is insufficient to conclude that  $^{62-66}\text{Cr}$  are good rotors because the  $Q(I)$  are average values that are insensitive to the shape fluctuations. We need to examine the properties of non-yrast states which are sensitive to shape fluctuation effects. We also note that  $Q(I)$  does not carry direct information about the ground state, and that, according to our calculation, the ground-state vibrational wave function is significantly different from those of the other yrast states with  $I \neq 0$ .

### C. Non-yrast states in $^{58-66}\text{Cr}$

To understand the nature of quadrupole collectivity, it is important to examine the properties of the excited bands including their interband transitions to the ground band, although they have not been observed experimentally yet. As typical examples of the calculated results, we display in Figs. 7 and 8 the excitation spectra and the  $B(E2)$  values of the low-lying states in  $^{60}\text{Cr}$  and  $^{64}\text{Cr}$ .

Let us first discuss the  $^{60}\text{Cr}$  case. We notice that the calculated excitation spectrum exhibits some features characteristic of the 5D harmonic oscillator (HO) limit; approximately equal level spacing in the ground band, approximate degeneracy of the  $4_1^+$  and  $2_2^+$  states, nearly equal values of  $B(E2; 0_2^+ \rightarrow 2_1^+)$  and  $B(E2; 4_1^+ \rightarrow 2_1^+)$ , which are about twice of  $B(E2; 2_1^+ \rightarrow 0_1^+)$ , etc. On the other hand, we also notice significant deviations from that limit. First, the  $0_2^+$  state is considerably lower than the  $4_1^+$  and  $2_2^+$  states. Second, the  $E2$  transitions forbidden in the HO limit are sizable; e.g., those from the  $2_2^+$  state to the  $4_1^+$  and  $0_2^+$  states are fairly large. Third,

the  $B(E2)$  value from the  $2_2^+$  state to the  $2_1^+$  state is less than half of those from the  $4_1^+$  and  $0_2^+$  states.

To examine the origin of these anharmonicities, let us look into the vibrational wave functions of the excited states. The  $\beta^4$ -weighted and non-weighted vibrational wave functions of the  $0_2^+$  and  $2_2^+$  states are displayed in Figs. 9 and 10, respectively. The  $0_2^+$  wave function exhibits two components: one around the spherical shape and the other around  $\beta = 0.35$ . Although it has a  $\beta$ -vibrational feature, i.e., a node in the  $\beta$  direction, it also exhibits a considerable deviation from the 5D HO limit, in which the deformed component concentrating on the prolate side would spread uniformly over the  $\gamma$  direction. We can see a deviation from the 5D HO limit also in the  $2_2^+$  state. The  $\beta^4$ -weighted  $2_2^+$  wave function spreads from the prolate to the oblate sides. However, the non-weighted wave function reveals that it also has the  $\beta$ -vibrational component. In fact, this state is a superposition of the large-amplitude  $\gamma$ -vibrational component spreading over the entire  $\gamma$  region and the  $\beta$ -vibrational component. In the 5D HO limit, the  $2_3^+$  wave function has a node in the  $\beta$  direction, while the  $2_2^+$  wave function has no node. The calculated  $2_2^+$  wave functions indicate significant mixing of these components. Thus, the low-lying states in  $^{60}\text{Cr}$  may be characterized as a quadrupole vibrational spectrum with strong anharmonicity.

Let us proceed to the  $^{64}\text{Cr}$  case. We immediately notice some features different from  $^{60}\text{Cr}$ . First, the approximate degeneracy of the  $4_1^+$  and  $2_2^+$  states seen in  $^{60}\text{Cr}$  is completely lifted here. Second, the  $E2$  transitions within the ground band are much stronger than those in  $^{60}\text{Cr}$ . Third, two low-lying excited bands appear: one consisting of the  $0_2^+$ ,  $2_2^+$  and  $4_2^+$  states (excited band I), and the other consisting of the  $2_3^+$ ,  $3_1^+$ ,  $4_3^+$  states (excited band II, the  $4_3^+$  state not shown here is at 2.84 MeV). One might be tempted to interpret these excited bands in terms of the conventional concept of the  $\beta$  and  $\gamma$  bands built on a well-deformed prolate ground state, but, in fact, they are markedly different from them. First, there is a strong mixing of the  $\beta$ - and  $\gamma$ -vibrational components, as seen from strong interband  $E2$  transitions between the two excited bands. Second, the calculated ratio of the excitation energies relative to  $E(0_2^+)$ ,  $(E(4_2^+) - E(0_2^+))/(E(2_2^+) - E(0_2^+))$ , is 2.51, which is far from the rigid-body value. Third, the  $K$ -mixing effects are strong, e.g., the  $K = 0$  ( $K = 2$ ) components of the  $2_2^+$  ( $2_3^+$ ) and  $4_2^+$  ( $4_3^+$ ) wave functions are at most 60%. To sum up, although the prolate deformation is appreciably developed in the low-lying states of  $^{64}\text{Cr}$ , the large-amplitude shape fluctuations play a dominant role and lead to the strong  $\beta - \gamma$  coupling and significant interband  $E2$  transitions.

In Fig. 11, we plot the vibrational wave functions at  $\gamma = 0.5^\circ$  and the probability density  $P(\beta)$  of finding a shape with a specific value of  $\beta$  for the ground and excited  $0^+$  states in  $^{60-64}\text{Cr}$ . Note that the probability density vanishes at the spherical shape because of the  $\beta^4$  factor in the volume element. It is seen that,

while the ground-state wave function for  $^{60}\text{Cr}$  distributes around the spherical shape, those for  $^{62}\text{Cr}$  and  $^{64}\text{Cr}$  extend from the spherical to deformed regions with  $\beta \simeq 0.4$  (see Fig. 11(a)). Accordingly, the peak of the probability distribution moves toward larger  $\beta$  in going from  $^{60}\text{Cr}$  to  $^{64}\text{Cr}$  (see Fig. 11(b)). Concerning the excited  $0^+$  states, their vibrational wave functions exhibit two peaks; a large peak at the spherical shape and a small peak at a prolate shape (see Fig. 11(c)). In the probability distribution displayed in Fig. 11(d), the spherical peaks moves to the  $\beta \approx 0.2$  region and the peaks at  $\beta = 0.35 - 0.4$  in turn become prominent.

The above results indicate that large-amplitude shape fluctuations play an important role both in the ground and excited  $0^+$  states. The growth of the shape fluctuations leads to an enhancement of the calculated  $E0$  transition strengths  $\rho^2(E0; 0_2^+ \rightarrow 0_1^+)$  in going from  $^{58}\text{Cr}$  to  $^{62-66}\text{Cr}$ , as displayed in Fig. 12.

#### D. Comparison with the (1+2)D calculation

To examine the role of dynamical shape fluctuations breaking the axial symmetry, we compare the above result of the (2+3)D calculation with the (1+2)D calculation where the axial symmetry is imposed. The procedure of the latter calculation is summarized in Appendix.

The obtained excitation energies,  $E2$  transitions and spectroscopic quadrupole moments are shown in Fig. 4. Obviously, the results of the (1+2)D calculation are more rotational than the (2+3)D results for all the isotopes; the  $R_{4/2}$  ratios, the  $B(E2)$  values and the magnitude of  $Q(2_1^+)$  are larger while the excitation energies are smaller. The difference is most remarkable in the  $R_{4/2}$  ratios. This implies that the neglect of the triaxial degree of freedom leads to spectra much closer to the rotational limit. In fact, the (1+2)D calculation considerably overestimates the experimental  $R_{4/2}$  values for  $^{60-64}\text{Cr}$ . The reason of this overestimation is easily understood in the following way. Let us first consider the  $\beta$ -rigid limit where  $\beta$  is fixed at a certain non-zero value,  $\beta = \beta_0$ . In this limit, the (1+2)D calculation obviously gives the axial rigid-rotor value 3.33 for  $R_{4/2}$ . On the other hand, in the (2+3)D calculation, the shape fluctuation in the  $\gamma$  degree of freedom is more or less always present. If the collective potential is flat in the  $\gamma$  direction, as in the Wilets-Jean model [27],  $R_{4/2}$  will be 2.50. In general,  $R_{4/2}$  will take a value between 2.50 and 3.33 in the  $\beta$ -rigid limit, depending on the softness of the collective potential toward the  $\gamma$  direction (see Figs. 3 and 4 in Ref. [28]). In reality, as a quantum system, the nuclear shape always fluctuates in both the  $\beta$  and  $\gamma$  directions. The experimental data that  $R_{4/2} \approx 2.68$  even in  $^{64}\text{Cr}$  clearly indicate that such shape fluctuations cannot be ignored. In the  $^{60}\text{Cr}$  case, the collective potential is quite soft in the  $\beta$  direction and the (2+3)D calculation yields  $R_{4/2} \approx 2.17$ . It is noteworthy that, even in such a situation, the  $2_1^+$  and  $4_1^+$  vibrational wave functions exhibit a localization about a

prolate shape (see Fig. 5). This is due to the dynamical effect minimizing the rotational energy for a given angular momentum.

### E. Similarities and differences with the Mg isotopes around $N = 20$

In Ref. [7], Lenzi et al. discussed similarities of the neutron-rich Cr isotopes near  $N = 40$  and the neutron-rich Mg isotopes around  $N = 20$ . Indeed, we have also found such similarities in our calculation. First of all, the growth of quadrupole collectivity in going from  $^{60}\text{Cr}$  to  $^{64}\text{Cr}$  is similar to that from  $^{30}\text{Mg}$  to  $^{32}\text{Mg}$ . In Fig. 6, while the ground state wave function in  $^{60}\text{Cr}$  distributes around the spherical shape, they are considerably extended to the prolately deformed region in  $^{64}\text{Cr}$ . The  $2_1^+$  wave function has a peak on the prolate side in  $^{60}\text{Cr}$  and it shifts to larger  $\beta$  in  $^{64}\text{Cr}$ . These features are similar to those seen in going from  $^{30}\text{Mg}$  to  $^{32}\text{Mg}$  in our calculation [21]. Concerning the excited  $0_2^+$  states in  $^{60}\text{Cr}$  and  $^{64}\text{Cr}$ , as shown in Figs. 11(c) and 11(d), both vibrational wave functions exhibit a two-hump structure. Similar two-hump structures of the excited  $0^+$  states have been obtained also in our calculation for  $^{30}\text{Mg}$  and  $^{32}\text{Mg}$ .

On the other hand, we have also found significant differences between the  $^{64}\text{Cr}$  region and the  $^{32}\text{Mg}$  region. First of all, the  $K$  mixing is strong in the excited bands in the Cr isotopes, whereas it is weak in the Mg region. The shape fluctuations toward the  $\gamma$  direction and the effect of the  $\beta - \gamma$  coupling are larger in the Cr isotopes than in Mg. This can be clearly seen, for instance, in the  $2_2^+$  wave functions displayed in Figs. 9 and 10.

## IV. CONCLUSIONS

In this paper, we have investigated the nature of the quadrupole collectivity in the low-lying states of neutron-rich Cr isotopes  $^{58-66}\text{Cr}$  by solving the 5D collective Schrödinger equation. The vibrational and rotational inertial functions and the collective potential in the 5D quadrupole collective Hamiltonian are microscopically derived with use of the CHFB+LQRPA method. The calculated inertial functions include the contributions from the time-odd components of the moving mean field. The results of calculation are in good agreement with the available experimental data. The prolate deformation remarkably develops along the isotopic chain from  $N = 36$  to 40. It is not appropriate, however, to characterize the low-lying state of Cr isotopes around  $^{64}\text{Cr}$  in terms of the prolate rigid-rotor model: the excitation spectra are still transitional and the large-amplitude shape fluctuations dominate in their low-lying states. The calculated excited bands exhibit strong couplings between the  $\beta$  and  $\gamma$  vibrational degrees of freedom. For close examination of the nature of quadrupole collectivity in these nuclei, experimental exploration of their excited bands is strongly

desired.

## Acknowledgments

The numerical calculations were carried out on SR16000 at Yukawa Institute for Theoretical Physics in Kyoto University and RIKEN Integrated Cluster of Clusters (RICC) facility. This work is supported by KAKENHI (Nos. 21340073, 23540294, and 23740223).

## Appendix

Here we summarize the procedure of the (1+2)D calculation to which the (2+3)D calculation reduces when the axial symmetry is imposed on the intrinsic shape. The dynamical variables in this reduced model are  $\beta$  and two Euler angles  $(\theta_1, \theta_2)$ , which describe the magnitude of the quadrupole deformation and the rotational motion perpendicular to the symmetry axis, respectively. The classical collective Hamiltonian of the (1+2)D model is given by

$$\mathcal{H}_{\text{coll}} = \frac{1}{2} \mathcal{M}_\beta(\beta) \dot{\beta}^2 + \frac{1}{2} \sum_{k=1,2} \mathcal{J}(\beta) \omega_k^2 + V(\beta), \quad (30)$$

where  $\omega_i$  are rotational frequencies related to the time derivative of the Euler angles. We quantize it according to the Pauli prescription, and then the collective Schrödinger equation reads

$$\left[ \hat{T}_{\text{vib}} + \sum_{k=1,2} \frac{\hat{I}_k^2}{2\mathcal{J}(\beta)} + V \right] \Psi_{\alpha IM}(\beta, \theta_1, \theta_2) = E_{\alpha I} \Psi_{\alpha IM}(\beta, \theta_1, \theta_2), \quad (31)$$

with

$$\hat{T}_{\text{vib}} = -\frac{1}{2M_\beta(\beta)} \frac{\partial^2}{\partial \beta^2} + \frac{1}{2M_\beta(\beta)} \left[ \frac{1}{2M_\beta(\beta)} \frac{\partial M_\beta(\beta)}{\partial \beta} - \frac{1}{\mathcal{J}(\beta)} \frac{\partial \mathcal{J}(\beta)}{\partial \beta} \right] \frac{\partial}{\partial \beta}. \quad (32)$$

The collective wave function can be written as a product of the vibrational and rotational wave functions:

$$\Psi_{\alpha IM}(\beta, \Omega) = \Phi_{\alpha I}(\beta) \langle \Omega | IM0 \rangle. \quad (33)$$

The collective Schrödinger equation in the intrinsic frame is

$$\left\{ \hat{T}_{\text{vib}} + \frac{I(I+1)}{2\mathcal{J}(\beta)} + V(\beta) \right\} \Phi_{\alpha I}(\beta) = E_{\alpha I} \Phi_{\alpha I}(\beta), \quad (34)$$

and the ortho-normalization condition is given by

$$\int d\beta \Phi_{\alpha I}^*(\beta) \Phi_{\alpha' I}(\beta) |G(\beta)|^{1/2} = \delta_{\alpha\alpha'} \quad (35)$$

with  $|G(\beta)| = M_\beta(\beta)\mathcal{J}^2(\beta)$ .

For the (1+2)D calculation with the P+Q model presented in subsection 3.3, we have used the same parameters as used in the (2+3)D calculation. In Ref. [22], the (1+2)D collective Schrödinger equation (34) was solved in the range  $-0.4 \leq \beta \leq 0.6$  without respecting the

boundary condition that the vibrational wave functions should satisfy at the spherical point (see Ref. [23]). In this paper, we have solved the collective Schrödinger equation in the range  $0 \leq \beta \leq 0.6$  respecting the boundary condition at  $\beta = 0$ . A detailed account on this point will be given in a future publication.

- 
- [1] O. Sorlin et al., *Eur. Phys. J. A* **16**, 55 (2003)
  - [2] A. Bürger et al., *Phys. Lett. B* **622**, 29 (2005)
  - [3] S. Zhu et al., *Phys. Rev. C* **74**, 064315 (2006)
  - [4] N. Aoi et al., *Nucl. Phys. A* **805**, 400c (2008).
  - [5] N. Aoi et al., *Phys. Rev. Lett.* **102**, 012502 (2009)
  - [6] A. Gade et al., *Phys. Rev. C* **81**, 051304(R) (2010)
  - [7] S. Lenzi, F. Nowacki, A. Poves, and K. Sieja, *Phys. Rev. C* **82**, 054301 (2010)
  - [8] H. Oba and M. Matsuo, *Prog. Theor. Phys.* **120**, 143 (2008).
  - [9] L. Gaodefroy, A. Obertelli, S. Péru, N. Pillet, S. Hilaire, J.-P. Delaroche, M. Girod, and J. Libert, *Phys. Rev. C* **80**, 064313 (2009).
  - [10] K. Kaneko, Y. Sun, M. Hasegawa and T. Mizusaki, *Phys. Rev. C* **78**, 064312 (2008).
  - [11] Y. Yang, Y. Sun, K. Kaneko, and M. Hasegawa, *Phys. Rev. C* **82**, 031304(R) (2010).
  - [12] M. Baranger and K. Kumar, *Nucl. Phys. A* **110**, 490 (1968)
  - [13] K. Kumar and M. Baranger, *Nucl. Phys. A* **110**, 529 (1968).
  - [14] N. Hinohara, T. Nakatsukasa, M. Matsuo and K. Matsuyanagi, *Prog. Theor. Phys.* **119**, 59 (2008).
  - [15] N. Hinohara, T. Nakatsukasa, M. Matsuo and K. Matsuyanagi, *Phys. Rev. C* **80**, 014305 (2009).
  - [16] N. Hinohara, K. Sato, T. Nakatsukasa, M. Matsuo, and K. Matsuyanagi, *Phys. Rev. C* **82**, 064313 (2010)
  - [17] M. Matsuo, T. Nakatsukasa and K. Matsuyanagi, *Prog. Theor. Phys.* **103**, 959 (2000).
  - [18] N. Hinohara, T. Nakatsukasa, M. Matsuo and K. Matsuyanagi, *Prog. Theor. Phys.* **117**, 451 (2007).
  - [19] K. Sato and N. Hinohara, *Nucl. Phys. A* **53**, 849 (2011)
  - [20] H. Watanabe et al., *Phys. Lett. B* **704**, 270 (2011)
  - [21] N. Hinohara, K. Sato, K. Yoshida, T. Nakatsukasa, M. Matsuo, and K. Matsuyanagi, *Phys. Rev. C* **84**, 061302 (2011)
  - [22] K. Yoshida and N. Hinohara, *Phys. Rev. C* **83**, 061302(R) (2011)
  - [23] K. Kumar and M. Baranger, *Nucl. Phys. A* **92**, 608 (1967)
  - [24] D. J. Thouless and J. G. Valatin, *Nucl. Phys.* **31**, 211 (1962)
  - [25] M. V. Stoitsov, J. Dobaczewski, W. Nazarewicz, and P. Ring, *Comp. Phys. Comm.* **167**, 43 (2005)
  - [26] H. Sakamoto and T. Kishimoto, *Phys. Lett. B* **245**, 321 (1990)
  - [27] L. Wilets and M. Jean, *Phys. Rev.* **102**, 788 (1956)
  - [28] K. Sato, N. Hinohara, T. Nakatsukasa, M. Matsuo, and K. Matsuyanagi, *Prog. Theor. Phys.* **123**, 129 (2010)
  - [29] W. Rother et al., *Phys. Rev. Lett.* **106**, 022502 (2011)



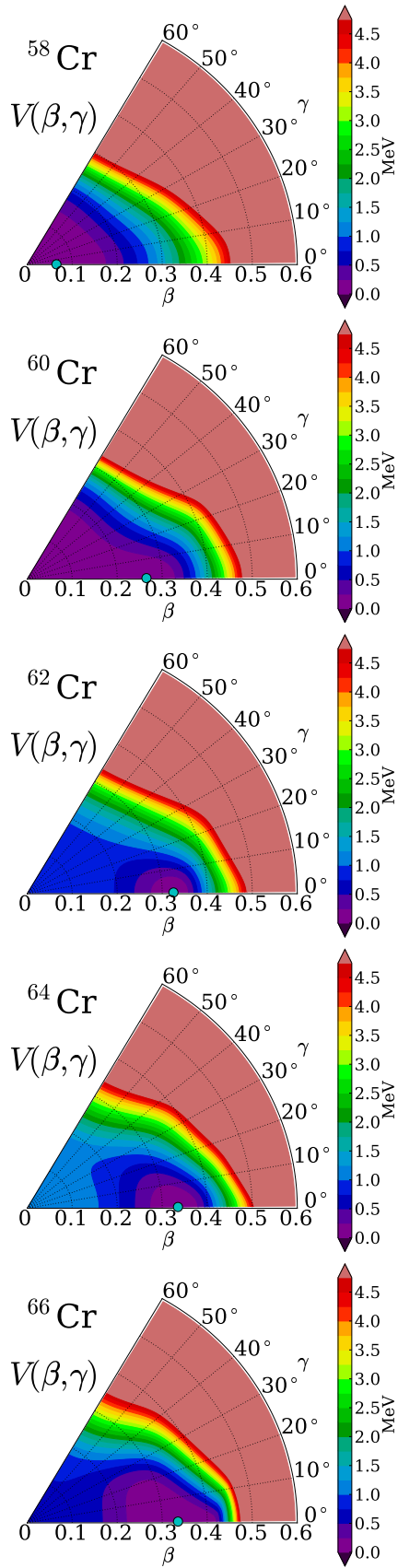


FIG. 1: (Color online) Collective potential energy surfaces  $V(\beta, \gamma)$  for  $^{58-66}\text{Cr}$ . The regions higher than 5 MeV (measured from the HFB minima) are colored rosy-brown.

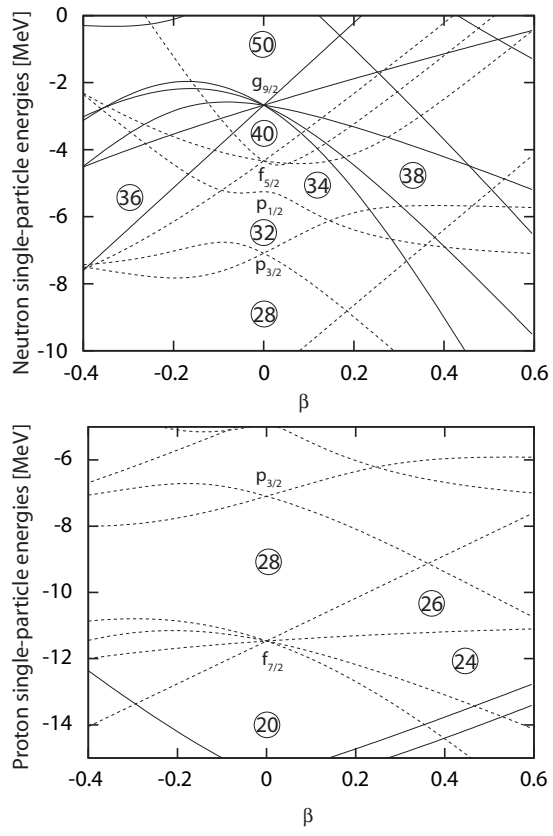


FIG. 2: Nilsson diagrams for neutrons (upper) and protons (lower) in  $^{62}\text{Cr}$  as functions of  $\beta$ , calculated as in Ref. [13]. The levels with the positive (negative) parity are plotted with solid (dotted) lines.

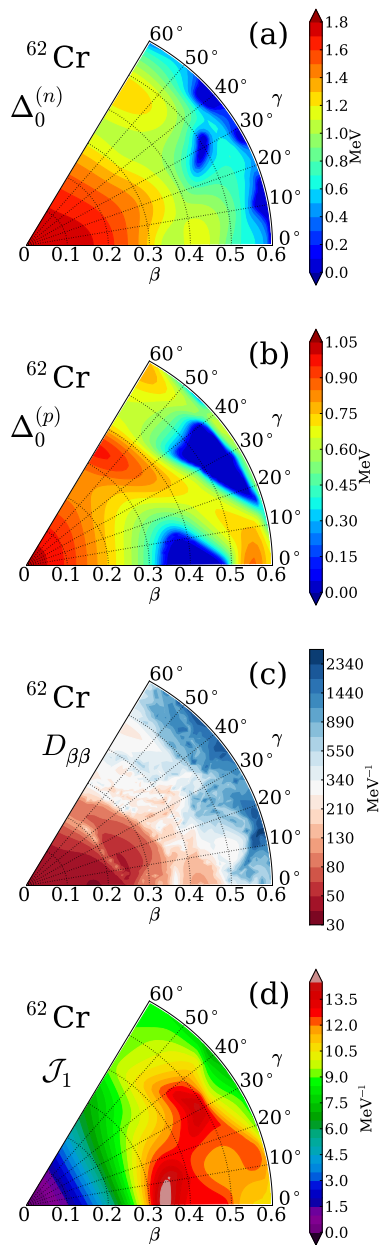


FIG. 3: (Color online) Neutron and proton monopole pairing gaps,  $\Delta_0^{(n)}(\beta, \gamma)$ ,  $\Delta_0^{(p)}(\beta, \gamma)$ , vibrational inertial function  $D_{\beta\beta}(\beta, \gamma)$ , and rotational moment of inertia  $\mathcal{J}_1(\beta, \gamma)$ , calculated for  $^{62}\text{Cr}$ .

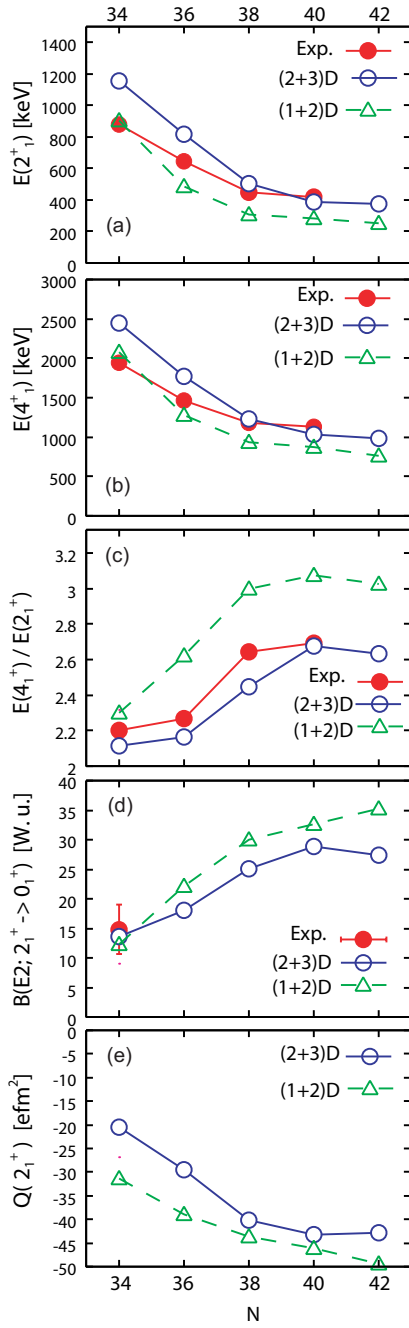


FIG. 4: (Color online) (a) Excitation energies of the  $2_1^+$  states for  $^{58-66}\text{Cr}$ . (b) Excitation energies of the  $4_1^+$  states. (c) Ratios of  $E(4_1^+)$  to  $E(2_1^+)$ . (d) Reduced  $E2$  transition probabilities  $B(E2; 2_1^+ \rightarrow 0_1^+)$  in Weisskopf units. (e) Spectroscopic quadrupole moments of the  $2_1^+$  states. Experimental data are taken from Refs. [2, 3, 5, 6].

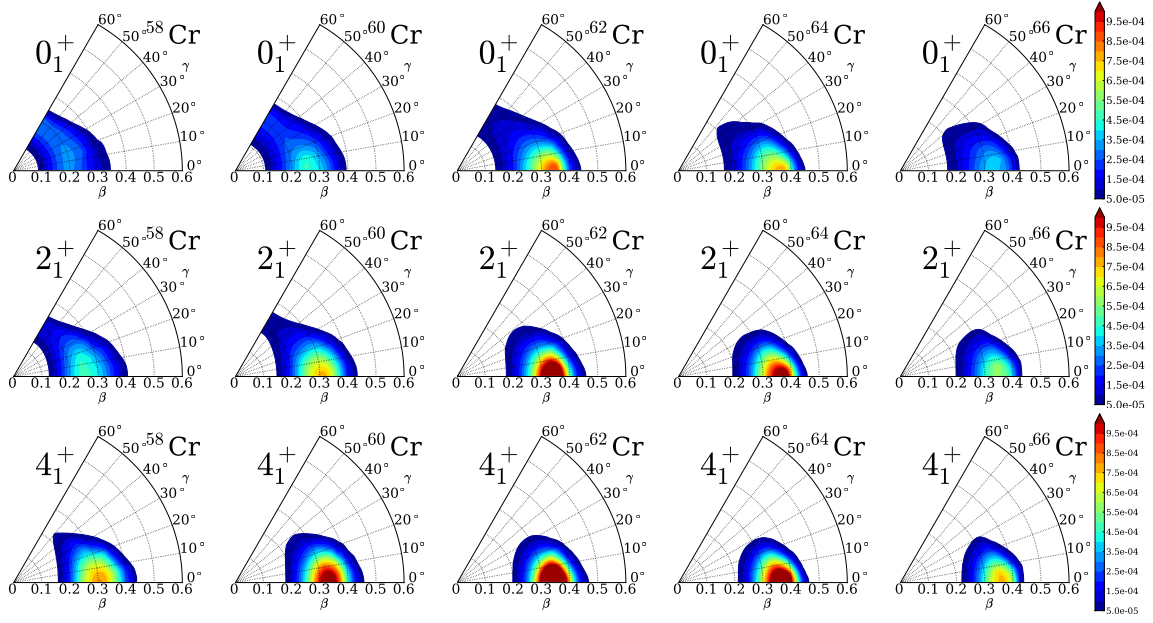


FIG. 5: (Color online) Squared vibrational wave functions multiplied by  $\beta^4$ ,  $\beta^4 \sum_K |\Psi_{\alpha IK}(\beta, \gamma)|^2$ , for the  $0_1^+$ ,  $2_1^+$  and  $4_1^+$  states in  $^{58-68}\text{Cr}$ .

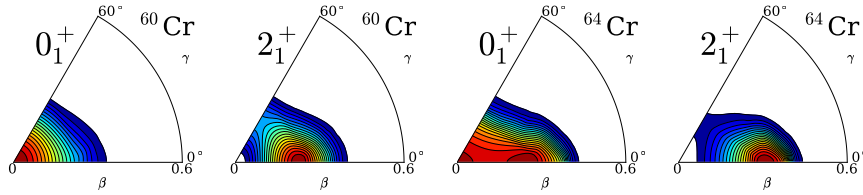


FIG. 6: (Color online) Vibrational wave function squared,  $\sum_K |\Psi_{\alpha IK}(\beta, \gamma)|^2$ , for the  $0_1^+$  and  $2_1^+$  states in  $^{60}\text{Cr}$  and  $^{64}\text{Cr}$ . The contour lines are drawn at every twentieth part of the maximum value.

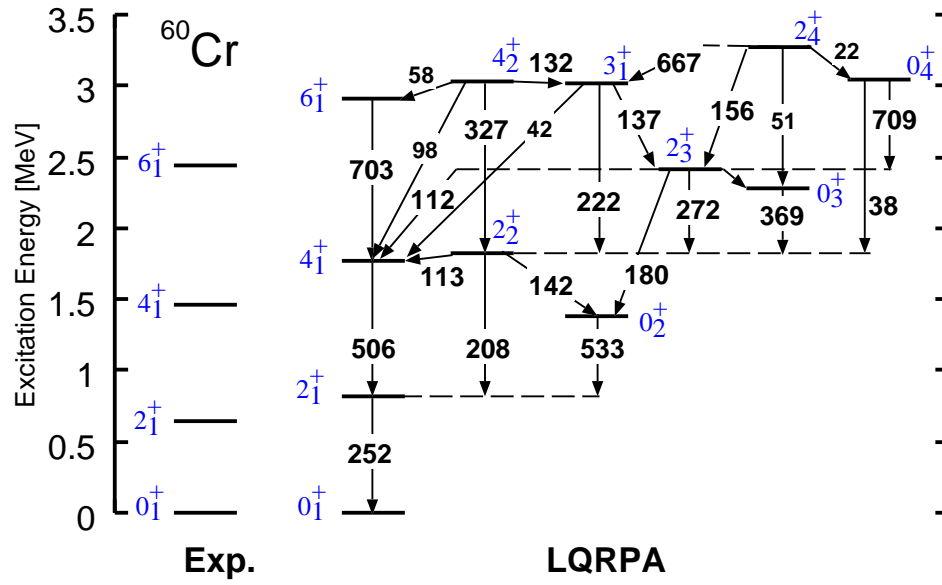


FIG. 7: (Color online) Excitation energies and  $B(E2)$  values for  $^{60}\text{Cr}$  in comparison with experimental data. Values on arrows indicate  $B(E2)$  in units of  $e^2\text{fm}^4$ . Only  $B(E2)$  values larger than 1 Weisskopf unit are shown. Experimental data are taken from Ref. [3].

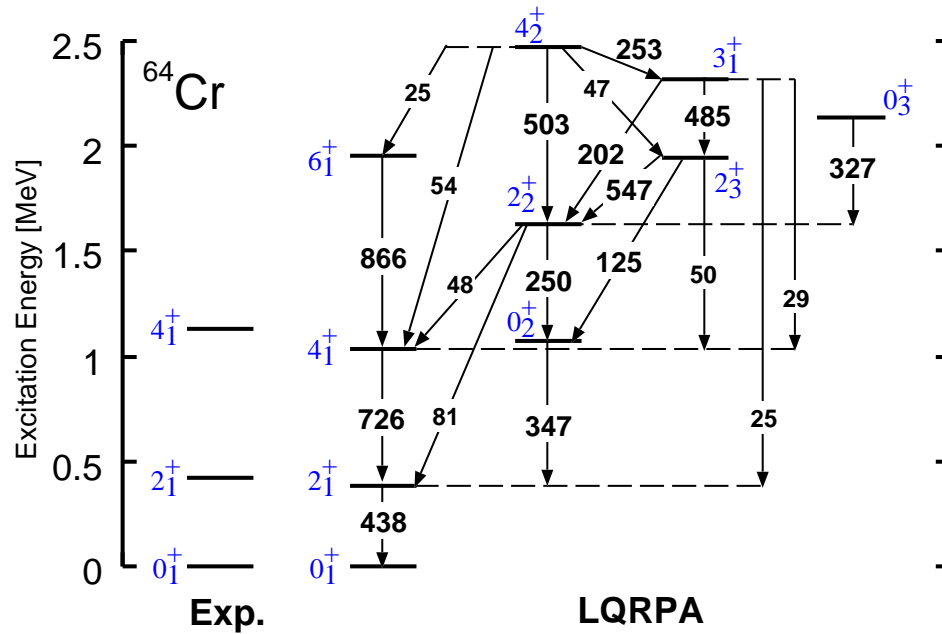


FIG. 8: (Color online) Same as Fig. 7 but for  $^{64}\text{Cr}$ . The experimental data are taken from Ref. [6].

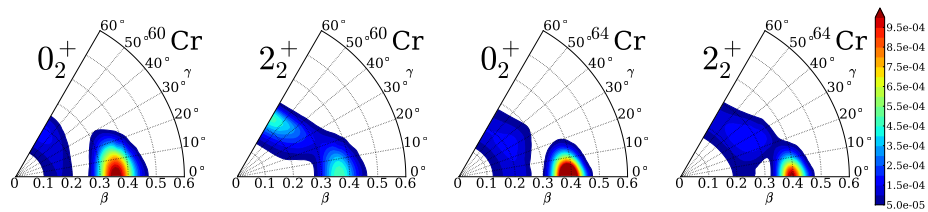


FIG. 9: (Color online) Squared vibrational wave functions multiplied by  $\beta^4$ ,  $\beta^4 \sum_K |\Psi_{\alpha IK}(\beta, \gamma)|^2$ , for the  $0_2^+$  and  $2_2^+$  states in  $^{60}\text{Cr}$  and  $^{64}\text{Cr}$ .

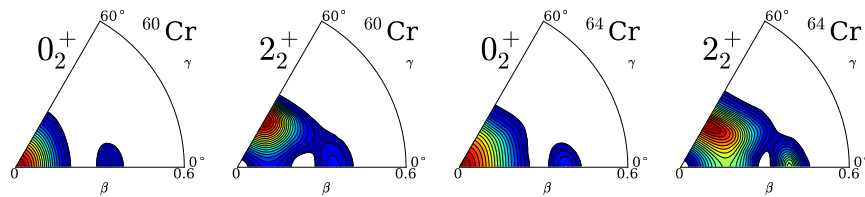


FIG. 10: (Color online) Same as Fig. 6 but for  $0_2^+$  and  $2_2^+$  states. The contour lines are drawn at every twentieth part of the maximum value.

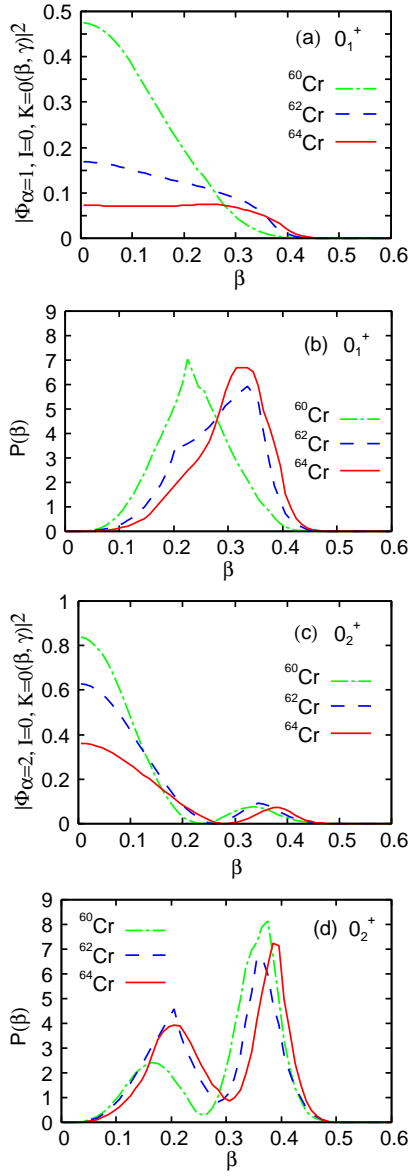


FIG. 11: (Color online) (a) Vibrational wave function squared  $|\Phi_{\alpha=1, I=0, K=0}(\beta, \gamma = 0.5^\circ)|^2$  of the ground states in  $^{60-64}\text{Cr}$ . (b) Probability densities integrated over  $\gamma$ ,  $P(\beta) = \int d\gamma |\Phi_{\alpha=1, I=0, K=0}(\beta, \gamma)|^2 |G(\beta, \gamma)|^{1/2}$ . (c) Same as (a) but for the  $0_2^+$  states. (d) Same as (b) but for the  $0_2^+$  states.



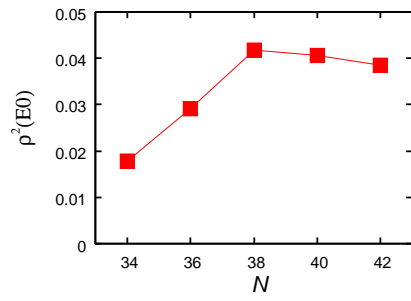


FIG. 12: (Color online)  $E0$  transition strengths  $\rho^2(E0; 0_2^+ \rightarrow 0_1^+)$  calculated for  $^{58-66}\text{Cr}$ .